

Detecting and braiding higher-order Majorana corner states through their spin degree of freedom

Xiao-Hong Pan, Xun-Jiang Luo, Jin-Hua Gao,^{*} and Xin Liu[†]

School of Physics and Institute for Quantum Science and Engineering,

Huazhong University of Science and Technology, Wuhan, Hubei 430074, China

*and Wuhan National High Magnetic Field Center and Hubei Key Laboratory of Gravitation and Quantum Physics,
Wuhan, Hubei 430074, China*



(Received 24 January 2022; revised 19 April 2022; accepted 20 April 2022; published 5 May 2022)

We uncover the transverse Majorana spin polarization of a class of higher-order topological superconductors. “Transverse” means that the spin polarization of the Majorana zero modes is perpendicular instead of parallel with the applied magnetic field. With this novel Majorana spin property, we predict the spin-selective Andreev reflection occurs at lead polarization perpendicular to the applied magnetic field, in sharp contrast to that in the Majorana nanowire and vortex system. The induced topological Josephson ϕ_0 junction shows the qualitative difference from the topologically trivial Josephson ϕ_0 junction and provides benefits in constructing all electronically controlled Majorana networks for braiding. We thus provide a comprehensive scheme for probing non-Abelian statistics in this class of higher-order topological superconductors with transverse Majorana spin texture.

DOI: [10.1103/PhysRevB.105.195106](https://doi.org/10.1103/PhysRevB.105.195106)

I. INTRODUCTION

Detecting and braiding Majorana zero modes (MZMs) is of the utmost urgency for any Majorana platform aiming at revealing their non-Abelian braiding statistics and implementing topological quantum computing [1–12]. This certainly applies to the recently developed higher-order topological superconductors (HOTSCs) [13–47] as well. For MZMs detection, it is now widely accepted that the zero-bias conductance peak (ZBCP) [48–56] alone is insufficient [57–63]. Meanwhile, the Majorana wave function is fully spin polarized [64–70] and gives rise to full spin-triplet superconducting correlation [71–75] even if the parent superconducting gap function is spin singlet. The resulting spin-selective Andreev reflection [65,67] and topological ϕ_0 junction [6,76–80] can serve as evidence of MZMs beyond the ZBCP. Remarkably, the latter can also measure the fermion-parity of two MZMs fusion [77] and is essential to implement the MZMs braiding [7,9,81–83]. However, as the Majorana polarization in the current experimental platforms is mainly parallel or antiparallel with the applied magnetic field, the trivial states may also induce similar transport phenomena with just quantitative difference [56].

Here, we found that the Majorana corner mode (MCM) spin polarization in a class of HOTSC is perpendicular to the applied magnetic field [Fig. 1(a)], referred to transverse Majorana spin polarization (MSP). The HOTSC consists of a two-dimensional topological insulator (2DTI) [84–88], an s-wave superconductor, and an in-plane magnetic field, all of which are experimentally feasible. The spin-selective Andreev reflection can be observed in the transverse direction

of the applied magnetic field. Remarkably, the Majorana coupling induced topological Josephson ϕ_0 junction performs qualitatively different from the topologically trivial ϕ_0 junction due to the transverse MSP. This is useful not only for detecting MCMs but also for the Majorana braiding and fermion parity measurement. Meanwhile, the existence of MCMs in this class of HOTSC is independent of the in-plane magnetic field direction [25], which imposes an additional parameter space for distinguishing MCMs and trivial states and brings significant advantages for constructing Majorana networks [Fig. 1(b)]. Based on this network, we provide a comprehensive scheme for braiding MCMs and probing their non-Abelian statistics in HOTSCs through a topological ϕ_0 junction.

This paper is organized as follows. In Sec. II, we show the transverse MCM spin polarization in the class of HOTSC. In Sec. III, we propose to detect the transverse MCM spin polarization through the ferromagnetic lead whose spin polarization is perpendicular to the magnetic field. In Sec. IV, we explore the effect of MCM spin texture on the Majorana coupling and the associative Josephson current. In Sec. V, we construct a Majorana network to braid MCMs.

II. SPIN TEXTURE OF MCMs

The class of HOTSC we study can be described by the Hamiltonian [25,31,34,35]

$$H(k) = H_c(k) + d_0(k)\tau_z s_0 \sigma_0, \quad (1)$$

where

$$H_c(k) = d_1(k)\tau_z s_0 \sigma_x + d_2(k)\tau_z s_0 \sigma_y + d_3(k)\tau_0 s_z \sigma_z + M(\cos \theta \tau_z s_x + \sin \theta \tau_0 s_y) \sigma_0 + \Delta \tau_y s_y \sigma_0, \quad (2)$$

with $d_{i=0,1,2,3}(k)$ depending on the specific models, such as Kane-Mele [84,85] and Bernevig-Hughes-Zhang

^{*}jinhua@hust.edu.cn

[†]phyliuxin@hust.edu.cn

TABLE I. Eigenbasis of chiral operators.

$(\epsilon_1, \epsilon_2)/\lambda$	+	-
(+, +)	$ \tau_y = +1\rangle \otimes \rightarrow\rangle$	$ \tau_y = -1\rangle \otimes \leftarrow\rangle$
(+, -)	$ \tau_y = -1\rangle \otimes \rightarrow\rangle$	$ \tau_y = +1\rangle \otimes \leftarrow\rangle$
(-, -)	$ \tau_y = +1\rangle \otimes \leftarrow\rangle$	$ \tau_y = -1\rangle \otimes \rightarrow\rangle$
(-, +)	$ \tau_y = -1\rangle \otimes \leftarrow\rangle$	$ \tau_y = +1\rangle \otimes \rightarrow\rangle$

models [86], Pauli matrices τ , s , and σ act on the Nambu, spin and orbital space, respectively (see details in Appendix A), M and Δ are magnitude of Zeeman splitting and s-wave pairing, respectively, and θ is the polar angle in the x - y plane indicating the direction of magnetic field. Note that the existence of MCMs is independent of the in-plane magnetic field direction [25,31,34,35]. Without loss of generality, we first take the magnetic field along y direction. The Hamiltonian of Eq. (1) has effective mirror symmetry $\hat{M}_x H(k_x, k_y) \hat{M}_x^{-1} = H(-k_x, k_y)$ and $\hat{M}_y H(k_x, k_y) \hat{M}_y^{-1} = H(k_x, -k_y)$ with $\hat{M}_x = i\tau_0 s_y \sigma_0$ and $\hat{M}_y = -i\tau_0 s_y \sigma_x$, respectively. Moreover, the Hamiltonian has inversion symmetry with $\hat{I} = \tau_0 s_0 \sigma_x$. If Ψ_1 is the wave function of the MCM γ_1 , the other three wave functions can be obtained as

$$(\Psi_2, \Psi_3, \Psi_4) = (\hat{M}_x, \hat{M}_y, \hat{I})\Psi_1. \quad (3)$$

Note that the Hamiltonian of Eq. (2) possess two chiral symmetries (Appendix A) with the symmetry operators

$$\mathcal{C}_1 = \tau_0 s_x \sigma_z \text{ and } \mathcal{C}_2 = \tau_y s_x \sigma_0. \quad (4)$$

The two chiral symmetry operators commute with each other and are block diagonal in orbital space. Therefore we can classify their eight common eigenbasis $\Phi_{(\epsilon_1, \epsilon_2)}^\lambda$ in Table I, with λ , ϵ_1 , and ϵ_2 the eigenvalues of σ_z , \mathcal{C}_1 and \mathcal{C}_2 , respectively, and \rightarrow (\leftarrow) indicates the spin along positive (negative) x direction. Due to the chiral symmetry, the MCMs must be the eigenstates of the chiral operators. Consequently, each MCM can be labeled by the eigenvalues (ϵ_1, ϵ_2) . Without loss of generality, we take the MCM at corner 1 [Fig. 1(a)] to have

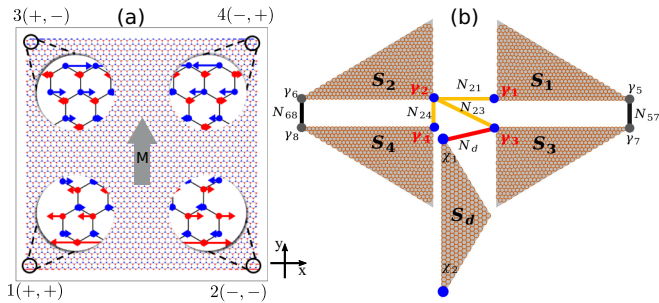


FIG. 1. (a) Fixing magnetic field along y , the transverse MSP distribution in bismuthene with chiral symmetry. The model parameters are taken from Ref. [89]. (b) Majorana network for braiding. The MCMs $\gamma_{1,2,3,4}$, $\chi_{1,2}$ sit on the HOTSC $S_{1,2,3,4,d}$. N_{21} , N_{23} , N_{24} are the normal wires to control the MCMs coupling. The MCMs $\gamma_{5,6,7,8}$ remain coupled through the wires N_{57} and N_{68} in the whole process. N_d is the normal wire connecting γ_3 and γ_1 which are used to detect the braiding result.

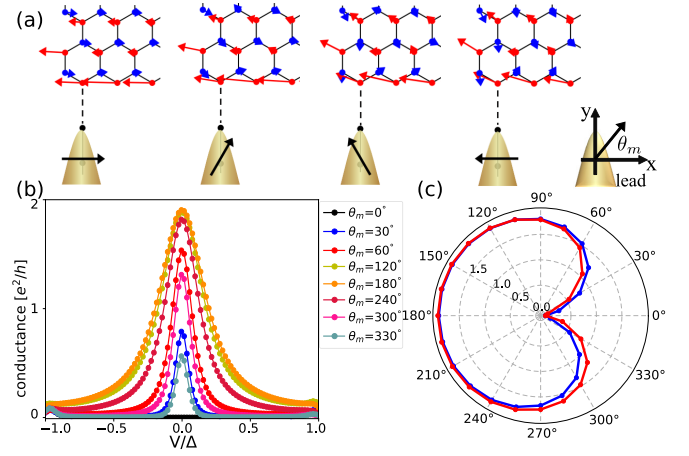


FIG. 2. The magnetic field is along y direction. (a) From left to right are the spin textures of the MCM with lead polarizations along 0° , 60° , 120° , and 180° , while the system possesses chiral symmetry. (b) is the conductance of MCMs at $k_B T = 0.03\Delta$. (c) The blue and red curves represent the relationship between the polarization direction and the height of zero bias conductance in the case of system with and without chiral symmetry, respectively.

eigenvalues of the chiral operators (+, +) as

$$\Psi_1(x, y) = g^+(x, y)\Phi_{(+,+)}^+ + g^-(x, y)\Phi_{(+,+)}^-, \quad (5)$$

where $g^{+(-)}(x, y)$ provide the spatial distribution of the wave function. Note that the spin polarization in the eight-basis is perpendicular to the magnetic field. To be concrete, we take the 2DTI to be bismuthene, which has a topologically non-trivial band gap of 0.5 eV [89–91]. The spin polarization of the four MCMs $\gamma_{i=1,2,3,4}$ with chiral symmetry is numerically calculated and shown in Fig. 1(a), which is consistent with our symmetry analysis. Here the $\lambda = +1$ and $\lambda = -1$ refer to the A (blue) and B (red) sublattices [Fig. 1(a)]. Breaking chiral symmetry, the MSP slightly deviates from the perpendicular direction of the magnetic field. Particularly, the stronger the magnetic field is, the more the MSP inclines to the vertical direction of the magnetic field. That is very different from the MSP parallel with the magnetic field in the semiconductor nanowire and vortex core. The above symmetry analysis can be applied to arbitrary in-plane magnetic field direction as discussed in Appendix A.

III. TRANSVERSE SPIN-SELECTIVE TUNNELING

The transverse MSP can be detected through the spin-selective Andreev reflection with the ferromagnetic lead polarization perpendicular to the magnetic field. Taking the magnetic field along the y direction, we first show the MSP of γ_1 with various lead polarizations in Fig. 2(a). The MSP remains unaffected for the lead polarization along the x direction. That implies the little coupling between the MCM and the lead. As varying the lead polarization from the x direction, the MSP deflects because the increased lead-MCM coupling breaks the chiral symmetry. That is consistent with our calculation of the finite-temperature conductance as varying the

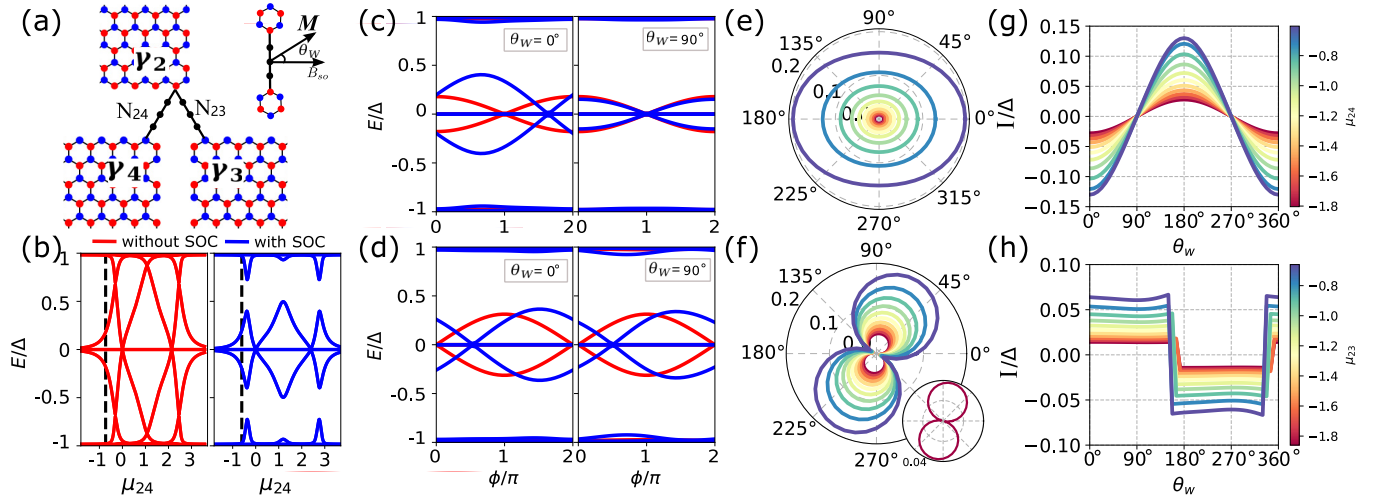


FIG. 3. (a) The configuration of the junction JJ_a and JJ_b , and θ_W is the angle between the magnetic field and spin-orbit coupling field B_{so} . (b) With $\theta_W = 0$, the red and blue curves are the Andreev levels at $\phi = 0$ as a function of the chemical potential μ_{24} in the wires N_{24} with $\lambda = 0$ and $\lambda \neq 0$ in JJ_a , respectively. (c) Given μ_{24} indicated by the black dot line in (b), the blue and red curves are the Andreev levels of JJ_a with $\lambda = 0$ and $\lambda \neq 0$ respectively. (d) The blue and red curves correspond to the Andreev levels of JJ_b with $\lambda = 0$ and $\lambda \neq 0$, respectively. (e) and (f) are the lowest positive eigenenergy of JJ_a and JJ_b as a function of θ_W at $\phi = 0$ respectively. (g) and (h) are the Josephson current as a function of θ_W in JJ_a and JJ_b at $\phi = 0$, respectively.

attached lead polarization (see details in Appendix B)

$$G_T(V) = -\frac{2e^2}{h} \int dE R(E) \frac{df(E-V)}{dE}, \quad (6)$$

with V the bias voltage, f the Fermi function, and $R(E)$ the probability of Andreev reflection obtained from the transport package Kwant [92]. We observed that the conductance reaches a minimum for the lead polarization being antiparallel to the MSP [Fig. 2(b)]. When the lead polarization deviates from this direction, the conductance rises rapidly to the saturation value [Fig. 2(b)] and becomes insensitive to the lead polarization at high conductance. That is more evident in our plot of the ZBCP in the polar coordinate [blue curves in Fig. 2(c)]. When the chiral symmetry is broken by the term $d_0(k)\tau_z\sigma_0s_0$, corresponding to the next-near-neighbor hopping in bismuthene, the spin texture is still roughly perpendicular to the direction of the magnetic field as shown in Fig. 7(b) in Appendix B. The lead polarization for the minimal ZBCP deviates from but is still close to the x direction [the red curves in Fig. 2(c)]. The high ZBCP shows similar behavior as when the system respects chiral symmetry. Therefore, spin-selective Andreev reflection responds to the applied magnetic field in the transverse direction, which is distinctive evidence for the MCMs in the class of HOTSC we are considering.

IV. MAJORANA COUPLING AND TOPOLOGICAL ϕ_0 JUNCTION

A topological Josephson junction, connecting two MCMs through a normal wire [Fig. 3(a)], can be used to detect and braid MZMs [9,93–100]. For simplicity, we consider the normal wire along y direction so that its Hamiltonian takes

$$H_{NW} = \frac{\hat{p}_y^2}{2m} + \lambda \hat{p}_y s_x, \quad (7)$$

where m is the effective mass and λ is the spin-orbit coupling (SOC) strength with the Rashba field B_{so} along the x direction. According to Eq. (A5), the two connected MCMs in our model are associated with either the effective mirror operator ($\Psi_2 = \hat{M}_y \Psi_4$) or inversion operator ($\Psi_2 = \hat{I} \Psi_3$). Taking $\lambda = 0$, our numerical calculation of the Andreev levels show $\cos(\phi/2)$ forms [red curves in Fig. 3(c)] for the former and $\cos(\phi + \pi)/2$ forms [red curves in Fig. 3(d)] for the latter with the magnetic field either perpendicular or parallel with the junction. We refer the former (latter) junction to JJ_a (JJ_b). Figure 3(b) shows that the Majorana coupling in JJ_a , indicated by the lowest positive eigenenergy at $\phi = 0$, can be tuned by the chemical potential inside the normal wire. Particularly, the Majorana coupling increases exponentially with the chemical potential of the normal wire approaching the band bottom from the insulating region (left region of the black dashed line). We found a similar result for the Majorana coupling in JJ_b at $\phi = \pi$. Therefore, we can turn on and off the Majorana coupling with exponential accuracy without fine tuning which is an essential condition for MZMs braiding [9,93–100]. When adding Rashba SOC in the normal wire, the Andreev crossing, in general, is shifted away from $\phi = 0$ or $\phi = \pi$, resulting in the finite Majorana coupling at $\phi = 0$ for both JJ_a and JJ_b [blue curves in Figs. 3(c) and 3(d)]. One exception happens in JJ_a [blue curves in Fig. 3(c)]: the Andreev crossing is unaffected by the SOC when the magnetic field is perpendicular to the SOC field. To understand these results, we project the Josephson junction Hamiltonian in MCMs Hilbert space. Note that the Rashba SOC induces the spin-dependent phase shift for particles transporting through the normal wire as [77] (see details in Appendix C)

$$\hat{T} = \tau_z e^{\frac{i}{2}\tau_z(\phi + \beta s_x)}, \quad (8)$$

with $\beta = 2m\lambda l/\hbar$ and l the nanowire length. We then obtain the MCMs coupling Hamiltonian

$$\begin{aligned}\tilde{H}_a &= i\tilde{t}\gamma_2\gamma_4\left(\sin\alpha_c\cos\frac{\beta}{2}\cos\frac{\phi}{2}-\cos\theta_W\sin\frac{\beta}{2}\sin\frac{\phi}{2}\right), \\ \tilde{H}_b &= i\tilde{t}\gamma_2\gamma_3\left(\cos\frac{\beta}{2}\sin\frac{\phi}{2}+\sin(\theta_W+\alpha_c)\sin\frac{\beta}{2}\cos\frac{\phi}{2}\right),\end{aligned}\quad (9)$$

where \tilde{t} is the effective hopping magnitude through the normal wire and θ_W is the angle between the magnetic field and B_{so} [Fig. 3(a)]. Here we introduce a phenomenological angle α_c to describe the MSP deviation from the perpendicular direction to the magnetic field due to the chiral symmetry breaking. The Majorana coupling Hamiltonians in Eq. (9) are fully consistent to our numerical plots: for $\beta = 0$, the Majorana coupling of JJ_a (JJ_b) is proportional to $\cos(\phi/2)$ [$\sin(\phi/2)$]; for finite SOC, $\beta \neq 0$, the Andreev level crossing generally is shifted from $\phi = 0$ or $\phi = \pi$, resulting in topological ϕ_0 junction; for JJ_a with $\theta_W = \pi/2$, the Andreev level crossing is always at $\phi = \pi$.

As we hope to control the Majorana coupling all electronically, meaning no flux in the system, hereafter we focus on the Majorana coupling and associated Josephson current at $\phi = 0$. According to Eq. (9), the Majorana coupling in this case takes

$$\begin{aligned}\tilde{H}_a &= i\tilde{t}\gamma_2\gamma_4\sin\alpha_c\cos\frac{\beta}{2}\cos\frac{\phi}{2}, \\ \tilde{H}_b &= i\tilde{t}\gamma_2\gamma_3\sin(\theta_W+\alpha_c)\sin\frac{\beta}{2}\cos\frac{\phi}{2}.\end{aligned}\quad (10)$$

Accordingly, the Majorana coupling for JJ_a and JJ_b does not explicitly and strongly depend on the magnetic field direction. We confirm these results by numerically calculating the lowest positive Andreev level (indicating the Majorana coupling) as a function of the magnetic field direction. In Fig. 3(e), the Majorana coupling for JJ_a shows a slight dependence on magnetic field direction. In Fig. 3(f), the Majorana coupling oscillates with varying the magnetic field direction and vanishes around $\theta_W = 0, \pi$. Note that if $\alpha_c = 0$, $\theta_W = 0, \pi$ means the MSP is along y or $-y$ direction because it is perpendicular to the magnetic field. In this case, the SOC induced spin-dependent phase $e^{i\beta s_x}$ has zero expectation value along the MSP direction. Therefore the Andreev level of JJ_b is not shifted by the SOC and should be proportional to $\sin(\phi/2)$, resulting in vanishing Majorana coupling.

Because the SOC shifts the Andreev level, the Josephson current is generally finite at $\phi = 0$ and takes the form

$$\begin{aligned}I_a &= \frac{e\tilde{t}}{\hbar}\cos\theta_W\sin\frac{\beta}{2}, \\ I_b &= \frac{e\tilde{t}}{\hbar}\text{sgn}(\sin(\theta_W+\alpha_c))\cos\frac{\beta}{2}.\end{aligned}\quad (11)$$

Accordingly, we expect that the Josephson current in JJ_a vanishes at $\theta_W = \pm\pi/2$ and peaks at $\theta_W = 0, \pi$; the Josephson current in JJ_b remains at constant amplitude and has a sudden sign change at the Andreev level crossing due to the term $\text{sgn}(\sin(\theta_W+\alpha_c))$. We then numerically calculate the Josephson current at zero temperature and $\phi = 0$ through the form

$$I = \frac{2e}{\hbar} \sum_{E_n < 0} \frac{\partial E_n}{\partial \phi} \Big|_{\phi=0},$$

with varying the magnetic field direction with different chemical potential in the normal wire. The numerically calculated current-phase relations is fully consistent with our theoretical prediction and are plotted in Fig. 3(g) and 3(h). Interestingly, the Josephson current I_b vanishes around $\theta_W \approx 0, \pi$ [Fig. 3(h)], at which the magnetic field is parallel with the SOC field direction. This is qualitatively different from the previous studies of topologically either trivial or nontrivial ϕ_0 junction. For the topologically trivial Josephson junction, although the combination of the magnetic field and SOC can also induce a ϕ_0 junction [77,101], its Josephson current at $\phi = 0$ peaks for the magnetic field parallel with the SOC field [77,101–104]. This result also holds in the topological ϕ_0 junction constructed by the spin-orbit coupled Majorana nanowire system [77]. This difference relies on the fact that the MSP is inclined to be perpendicular to the magnetic field in our model. Therefore, observing the Josephson current at $\phi = 0$ in JJ_b can provide strong evidence for system entry into the topological region. Besides, the eigenstates of the Majorana coupling Hamiltonian in Eq. (10) are also the eigenstates of the fermion parity operator. For example, the two blue curves near the Fermi surface in Fig. 3(d), corresponding to the even and odd fermion parity according to Eq. (9), has an opposite slope at $\phi = 0$, carrying opposite Josephson current. Therefore, observing Josephson current direction can reflect the fermion parity of the two MCMs connected by the junction.

V. BRAIDING MCMS

Majorana couplings can provide the holonomic protocol of braiding MZMs [77,81,93] in the Majorana network [Fig. 1(b)]. We will braid the MCMs γ_3 and γ_4 and measure the fermion parity of $i\gamma_3\chi_1$ before and after the braiding to test the non-Abelian statistics. We first initialize the state to the fermion parity eigenstates of $i\gamma_3\chi_1$ by measuring the Josephson current direction through N_d [Fig. 1(b)]. Then the braiding process is divided into three intervals: In the first interval, we tune μ_{24} and μ_{21} to exponentially turn on and off the coupling of $\gamma_2 - \gamma_4$ and $\gamma_2 - \gamma_1$, respectively [Fig. 4(a)] so that the MCM at the γ_4 position is moved to the γ_1 position [Fig. 4(b)]; In the second interval, we tune μ_{23} and μ_{24} to exponentially turn on and off the coupling of $\gamma_2 - \gamma_3$ and $\gamma_2 - \gamma_4$, respectively [Fig. 4(a)] so that the MCM at the γ_3 position is moved to the γ_4 position [Fig. 4(b)]; In the final interval, we tune μ_{21} and μ_{23} to exponentially turn on and off the coupling of $\gamma_2 - \gamma_1$ and $\gamma_2 - \gamma_3$, respectively [Fig. 4(a)] so that the MCM at γ_1 position is moved to γ_3 position [Fig. 4(b)]. During the braiding process, the energy of the two MZMs remains zero as indicated by the red line in Fig. 4(b) and separated from excited states by a finite energy gap. The non-Abelian berry phase accumulated in the braiding process can be revealed through the path-ordered Wilson loop calculation in the MCMs basis $(\Psi_3(t), \Psi_4(t))^T$ [105–107]

$$\begin{aligned}U &= \mathcal{P}e^{-\oint d\mu A(t)} = \prod_{n=0}^{N-1} \sum_{\alpha, \beta=3}^4 (\Psi_\alpha(t_n) | \Psi_\beta(t_{n+1})) \\ &= a_0\eta_0 + a_x\eta_x + a_y\eta_y + a_z\eta_z,\end{aligned}\quad (12)$$

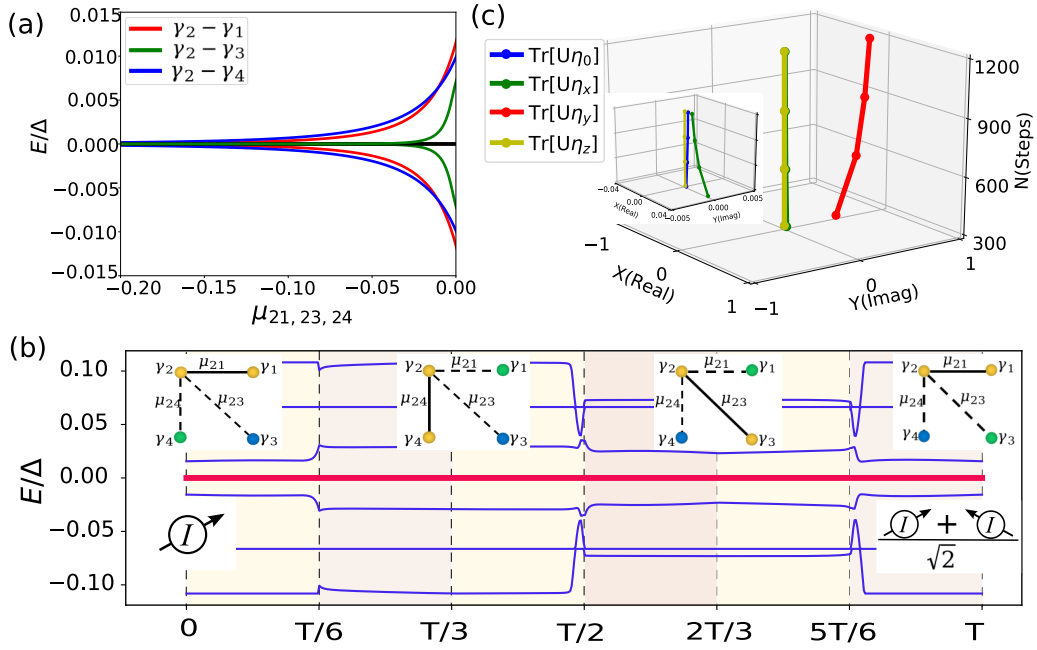


FIG. 4. (a) The relationship between chemical potential μ_{21} , μ_{23} , μ_{24} and the Majorana coupling magnitude of $\gamma_2 - \gamma_1$, $\gamma_2 - \gamma_3$ and $\gamma_2 - \gamma_4$, respectively. (b) The energy spectrum in the whole procedure of exchanging γ_3 and γ_4 . The insets characterize the exchange protocol of $\gamma_3 \leftrightarrow \gamma_4$. The ammeters indicate the Josephson current through N_d for the initial and final states of the braiding process. (c) The relationship between the coefficients (a_0 , a_x , a_y , a_z) and the total steps.

where $t_{n+1} - t_n = T/N$, N is the total steps for exchanging the MCMs in period T and η is the Pauli matrix acting on the basis $(\Psi_3(0), \Psi_4(0))^T$. Our numerical calculation shows that the braiding matrix U has only finite η_y component whose amplitude approaches i with increasing the total steps N [Fig. 4(c)]. This is consistent with the well-known MZMs exchanging, $\gamma_3 \rightarrow -\gamma_4$ and $\gamma_4 \rightarrow \gamma_3$, reflecting the feasibility of our all-electronically controlled braiding proposal. The experimental detection of the non-Abelian statistics can be performed through measuring the Josephson current after the braiding. As the state is initialized to the parity eigenstates of $i\gamma_3\chi_1$, it will have 50% probability to observe the current direction switch after the successful MCMs braiding [77].

VI. CONCLUSION

In summary, we provide a comprehensive scheme to detect and braid a class of MCMs in HOTSC using their unique spin properties. As the spin polarization of MCMs in this class is perpendicular to the magnetic field, the associated spin-dependent properties are qualitatively different from those in first-order TSC and topologically trivial superconductors. These can provide strong evidence that the system is in the HOTSC phase. We then present an all-electronically controlled Majorana network and numerically simulate the braiding process. Our scheme is shown in a realistic bismuth model but is also applicable to other Kane-Mele or BHZ model-based materials.

ACKNOWLEDGMENTS

We thank X.-J. Liu, C.-X. Liu, and D. E. Liu for fruitful discussions. X.L. acknowledges the support of National

Natural Science Foundation of China (Grant No. 12074133, Grant No. 11674114) and National Key R&D Program of China (Grant No. 2016YFA0401003). J.-H.G. acknowledges the support of National Natural Science Foundation of China (Grants No. 11874160, No. 12141401, and No. 11534001), National Key R&D Program of China (2017YFA0403501), and the Fundamental Research Funds for the Central Universities (HUST: 2017KFYXJJ027).

APPENDIX A: FERRIMAGNETIC SPIN TEXTURE UNDER ARBITRARY IN-PLANE MAGNETIC FIELD

The class of HOTSC, realized by 2D TI in proximity to s-wave superconductor under in-plane magnetic field, can be generally described by a minimal Hamiltonian

$$H(k) = H_c(k) + d_0(k)\tau_z s_0 \sigma_0,$$

where

$$H_c(k) = d_1(k)\tau_z s_0 \sigma_x + d_2(k)\tau_z s_0 \sigma_y + d_3(k)\tau_0 s_z \sigma_z + M(\cos \theta \tau_z s_x + \sin \theta \tau_0 s_y) \sigma_0 + \Delta \tau_y s_y \sigma_0. \quad (\text{A1})$$

The coefficients $d_{0,1,2,3}$ depend on specific models. In Kane-Mele [84,85] model, the coefficients take the form

$$d_0(k) = -2t_2 \left(\cos \sqrt{3}k_x + 2 \cos \frac{\sqrt{3}}{2}k_x \cos \frac{3}{2}k_y \right);$$

$$d_1(k) = -t \left(\cos k_y + 2 \cos \frac{1}{2}k_y \cos \frac{\sqrt{3}}{2}k_x \right);$$

TABLE II. Eigenbasis of \mathcal{C}_1 and \mathcal{C}_2 .

$\lambda/(\epsilon_1, \epsilon_2)$	(+, +)	(+, -)	(-, +)	(-, -)
+	$\begin{bmatrix} e^{-i\frac{\theta}{2}} \begin{bmatrix} 1 \\ e^{i(\theta+\frac{3\pi}{2})} \end{bmatrix}_s \\ e^{i\frac{\theta}{2}} \begin{bmatrix} 1 \\ e^{i(\theta+\frac{3\pi}{2})} \end{bmatrix}_s^* \\ e^{-i\frac{\theta+\pi}{2}} \begin{bmatrix} 1 \\ e^{i(\theta+\frac{\pi}{2})} \end{bmatrix}_s \\ e^{i\frac{\theta+\pi}{2}} \begin{bmatrix} 1 \\ e^{i(\theta+\frac{\pi}{2})} \end{bmatrix}_s^* \end{bmatrix}$	$\begin{bmatrix} e^{-i\frac{\theta+\pi}{2}} \begin{bmatrix} 1 \\ e^{i(\theta+\frac{3\pi}{2})} \end{bmatrix}_s \\ e^{i\frac{\theta+\pi}{2}} \begin{bmatrix} 1 \\ e^{i(\theta+\frac{3\pi}{2})} \end{bmatrix}_s^* \\ e^{-i\frac{\theta}{2}} \begin{bmatrix} 1 \\ e^{i(\theta+\frac{\pi}{2})} \end{bmatrix}_s \\ e^{i\frac{\theta}{2}} \begin{bmatrix} 1 \\ e^{i(\theta+\frac{\pi}{2})} \end{bmatrix}_s^* \end{bmatrix}$	$\begin{bmatrix} e^{-i\frac{\theta+\pi}{2}} \begin{bmatrix} 1 \\ e^{i(\theta+\frac{\pi}{2})} \end{bmatrix}_s \\ e^{i\frac{\theta+\pi}{2}} \begin{bmatrix} 1 \\ e^{i(\theta+\frac{\pi}{2})} \end{bmatrix}_s^* \\ e^{-i\frac{\theta}{2}} \begin{bmatrix} 1 \\ e^{i(\theta+\frac{3\pi}{2})} \end{bmatrix}_s \\ e^{i\frac{\theta}{2}} \begin{bmatrix} 1 \\ e^{i(\theta+\frac{3\pi}{2})} \end{bmatrix}_s^* \end{bmatrix}$	$\begin{bmatrix} e^{-i\frac{\theta}{2}} \begin{bmatrix} 1 \\ e^{i(\theta+\frac{\pi}{2})} \end{bmatrix}_s \\ e^{i\frac{\theta}{2}} \begin{bmatrix} 1 \\ e^{i(\theta+\frac{\pi}{2})} \end{bmatrix}_s^* \\ e^{-i\frac{\theta+\pi}{2}} \begin{bmatrix} 1 \\ e^{i(\theta+\frac{3\pi}{2})} \end{bmatrix}_s \\ e^{i\frac{\theta+\pi}{2}} \begin{bmatrix} 1 \\ e^{i(\theta+\frac{3\pi}{2})} \end{bmatrix}_s^* \end{bmatrix}$
-	$\begin{bmatrix} e^{-i\frac{\theta}{2}} \begin{bmatrix} 1 \\ e^{i(\theta+\frac{3\pi}{2})} \end{bmatrix}_s \\ e^{i\frac{\theta}{2}} \begin{bmatrix} 1 \\ e^{i(\theta+\frac{3\pi}{2})} \end{bmatrix}_s^* \\ e^{-i\frac{\theta+\pi}{2}} \begin{bmatrix} 1 \\ e^{i(\theta+\frac{\pi}{2})} \end{bmatrix}_s \\ e^{i\frac{\theta+\pi}{2}} \begin{bmatrix} 1 \\ e^{i(\theta+\frac{\pi}{2})} \end{bmatrix}_s^* \end{bmatrix}$	$\begin{bmatrix} e^{-i\frac{\theta+\pi}{2}} \begin{bmatrix} 1 \\ e^{i(\theta+\frac{3\pi}{2})} \end{bmatrix}_s \\ e^{i\frac{\theta+\pi}{2}} \begin{bmatrix} 1 \\ e^{i(\theta+\frac{3\pi}{2})} \end{bmatrix}_s^* \\ e^{-i\frac{\theta}{2}} \begin{bmatrix} 1 \\ e^{i(\theta+\frac{\pi}{2})} \end{bmatrix}_s \\ e^{i\frac{\theta}{2}} \begin{bmatrix} 1 \\ e^{i(\theta+\frac{\pi}{2})} \end{bmatrix}_s^* \end{bmatrix}$	$\begin{bmatrix} e^{-i\frac{\theta+\pi}{2}} \begin{bmatrix} 1 \\ e^{i(\theta+\frac{\pi}{2})} \end{bmatrix}_s \\ e^{i\frac{\theta+\pi}{2}} \begin{bmatrix} 1 \\ e^{i(\theta+\frac{\pi}{2})} \end{bmatrix}_s^* \\ e^{-i\frac{\theta}{2}} \begin{bmatrix} 1 \\ e^{i(\theta+\frac{3\pi}{2})} \end{bmatrix}_s \\ e^{i\frac{\theta}{2}} \begin{bmatrix} 1 \\ e^{i(\theta+\frac{3\pi}{2})} \end{bmatrix}_s^* \end{bmatrix}$	$\begin{bmatrix} e^{-i\frac{\theta}{2}} \begin{bmatrix} 1 \\ e^{i(\theta+\frac{\pi}{2})} \end{bmatrix}_s \\ e^{i\frac{\theta}{2}} \begin{bmatrix} 1 \\ e^{i(\theta+\frac{\pi}{2})} \end{bmatrix}_s^* \\ e^{-i\frac{\theta+\pi}{2}} \begin{bmatrix} 1 \\ e^{i(\theta+\frac{3\pi}{2})} \end{bmatrix}_s \\ e^{i\frac{\theta+\pi}{2}} \begin{bmatrix} 1 \\ e^{i(\theta+\frac{3\pi}{2})} \end{bmatrix}_s^* \end{bmatrix}$

$$d_2(k) = -t \left(\sin k_y - 2 \sin \frac{1}{2} k_y \cos \frac{\sqrt{3}}{2} k_x \right);$$

$$d_3(k) = -2\lambda_{\text{soc}} \left(\sin \sqrt{3} k_x - 2 \sin \frac{\sqrt{3}}{2} k_x \cos \frac{3}{2} k_y \right), \quad (\text{A2})$$

where $t, t_2, \lambda_{\text{soc}}$ are the magnitudes of nearest hopping, next-nearest hopping, and SOC, respectively. In the Bernevig-Hughes-Zhang model [86], the coefficients take the form

$$\begin{aligned} d_0(k) &= C + 2t_{x0}(1 - \cos k_x) + 2t_{y0}(1 - \cos k_y); \\ d_1(k) &= m_0 + 2t_x(1 - \cos k_x) + 2t_y(1 - \cos k_y); \\ d_2(k) &= A_y \sin k_y; \\ d_3(k) &= A_x \sin k_x, \end{aligned} \quad (\text{A3})$$

where $C, t_{x(y)0}, m_0, t_{x(y)}, A_{x(y)}$ are the parameter determined the kinetic energy. For arbitrary in-plane magnetic field direction $\mathbf{M}(\cos \theta \tau_z s_x + \sin \theta \tau_0 s_y) \sigma_0$, the Hamiltonian possesses mirror symmetry and inversion symmetry, which takes the form as

$$\begin{aligned} M_x &= i(\cos \theta \tau_z s_x + \sin \theta \tau_0 s_y) \sigma_0, \\ M_y &= -i(\cos \theta \tau_z s_x + \sin \theta \tau_0 s_y) \sigma_x, \\ I &= \tau_0 s_0 \sigma_x. \end{aligned} \quad (\text{A4})$$

If Ψ_1 is the wave function of the MCM γ_1 , the other three wave functions can be obtained as

$$(\Psi_2, \Psi_3, \Psi_4) = (\hat{M}_x, \hat{M}_y, \hat{I})\Psi_1. \quad (\text{A5})$$

Notably, ignoring the $d_0(k)$ term, the Hamiltonian possesses two chiral symmetry operators, which can be expressed as

$$\begin{aligned} \mathcal{C}_1 &= \sin \theta \tau_0 s_x \sigma_z - \cos \theta \tau_z s_y \sigma_z, \\ \mathcal{C}_2 &= \tau_y s_x \sigma_0. \end{aligned} \quad (\text{A6})$$

The two chiral symmetry operators commute with each other and are block diagonal in orbital space. Therefore we can classify their eight common eigenbases $\Phi_{(\epsilon_1, \epsilon_2)}^\lambda$ as shown in Table II. Here, λ, ϵ_1 , and ϵ_2 are the eigenvalue of σ_z, \mathcal{C}_1 , and \mathcal{C}_2 respectively. For the eigenstates with the same eigenvalue (ϵ_1, ϵ_2) , the spin textures at orbital $\lambda = +$ and $\lambda = -$ are always in opposite directions and both differ by $\pm\pi/2$ from the magnetic field direction θ . Without loss of generality, we now consider the MCM at corner 1 has the eigenvalues $(\mathcal{C}_1 = +1, \mathcal{C}_2 = +1)$ which gives the wave function

$$\Psi_1(x, y) = g(x, y)^+ \Phi_{(+, +)}^+ + g(x, y)^- \Phi_{(+, +)}^-, \quad (\text{A7})$$

where $g(x, y)^\pm$ provides the spatial distribution of the wave function. The other three wave functions (Ψ_2, Ψ_3, Ψ_4) can be obtained through acting mirror or inversion operation on Ψ_1 . Obviously, from the wave function above, the spin texture of the MCMs are both perpendicular to the magnetic field and hold opposite directions at the different orbitals. By fixing the magnetic field along $+y$ direction $\theta = \pi/2$, the Majorana spin polarizations are along $\pm x$ direction as shown in the main text. To further verify this result, we plot the total Majorana spin polarization as a function of magnetic field direction for $\lambda = \pm 1$ with the 2D TIs taking Kane-Mele [84,85], bismuthene [89–91], and Bernevig-Hughes-Zhang models [86], respectively. As shown in Fig. 5, the total spin polarization of the MCMs are perpendicular to \mathbf{M} and in opposite directions at orbitals $\lambda = \pm 1$, which are consistent with our analysis. Below we take the 2D TI model as the bismuthene model, which has a topologically nontrivial band gap of about 0.5 eV.

APPENDIX B: SPIN-SELECTIVE TUNNELING OF THE SYSTEM BREAKING CHIRAL SYMMETRY

To detect the MCM spin polarization, we attach a ferromagnetic lead to the system. The Hamiltonian of the ferromagnetic lead takes

$$\begin{aligned} H_{\text{lead}} &= \left(\frac{\hbar^2 k^2}{2m} - \mu_l \right) \tau_z s_0 + \lambda_{\text{ex}} (\cos \theta_m \tau_z s_x + \sin \theta_m \tau_0 s_y) \\ &\quad + V_{\text{ex}} (\tau_z s_0 - \cos \theta_m \tau_z s_x - \sin \theta_m \tau_0 s_y), \end{aligned} \quad (\text{B1})$$

where μ_l, θ_m , and λ_{ex} are the lead chemical potential, the lead polarization angle in the x - y plane and the magnitude of Zeeman splitting. Here, the term proportional to V_{ex} is used to separate the two spin channels to simulate the system with the single spin channel as shown in Fig. 6(c). The zero-temperature conductance is calculated through

$$G_0 = \frac{e^2}{h} (1 - R_{ee} + R_{eh}), \quad (\text{B2})$$

where R_{ee}, R_{eh} are the probability of normal reflection and Andreev reflection which can be obtained through the transport package Kwant [92]. The finite temperature conductance takes the form

$$G_T(V) = - \int dE G_0 \frac{df(E - V)}{dE}, \quad (\text{B3})$$

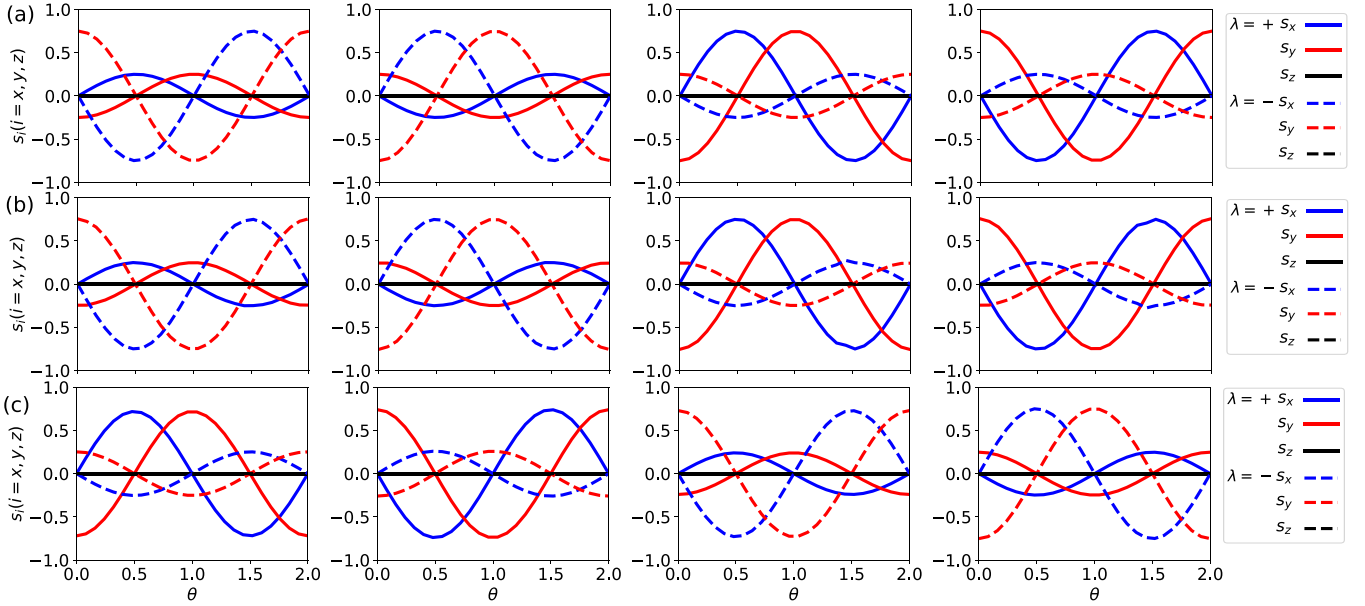


FIG. 5. From left to right are the total spin polarization of MCMs which are localized at corners 1, 2, 3, and 4, respectively in the class of HOTSC as the function of in-plane magnetic field direction. (a), (b), and (c) are corresponding to the 2D TI in the HOTSCs taken to be Kane-Mele, bismuthene, and BHZ models, respectively. We set the nearest hopping magnitude $t=1$ and the magnitude of the next nearest spin-orbital coupling $\lambda_{so}/3\sqrt{3} = 0.26$ in Kane-Mele model. The parameters selected in bismuthene are according to Ref. [91].

where V and f are the bias voltage and Fermi function, respectively. Considering the next-nearest-neighbor hopping term, the system breaks chiral symmetry and thus displays asymmetry electronic energy spectrum as plotted in Fig. 6(a). The spin texture is not strictly but still roughly perpendicular to the direction of the magnetic field as shown in Fig. 6(b). The conductance at finite temperature still reaches a minimum when the lead polarization is close to the x direction as shown in Fig. 6(d).

APPENDIX C: TOPOLOGICAL AND TRIVIAL ϕ_0 JUNCTION

1. Topological ϕ_0 junction constructed by HOTSCs with chiral symmetry

In this section, we consider the two MCMs coupling through a normal wire with Rashba SOC. Generally, the Zeeman splitting energy in the wire is much smaller than the Rashba SOC. For simplicity, we first consider the wire without Zeeman splitting. The Hamiltonian of the normal wire can be

expressed as [77]

$$H_W = \sum_i 2t_w s_0 C_i^\dagger C_i + C_{i+1}^\dagger (-t_w s_0 - i\lambda s_x) C_i, \quad (C1)$$

where t_w , λ are the magnitude of nearest-hopping and Rashba SOC, respectively. The coupling Hamiltonian between the normal wire and the system takes the form

$$\begin{aligned} H_t^u &= -t_w s_0 C_u^\dagger C_1 + \text{h.c.}, \\ H_t^d &= -t_w s_0 C_d^\dagger C_l + \text{h.c.}, \end{aligned} \quad (C2)$$

with u and d the end sites of HOTSCs which are connected through the wire. The normal SOC wire contributes an effective self-energy

$$\Sigma = -H_t G_{\text{soc}} H_t^\dagger \quad (C3)$$

with $H_t = (H_t^u, H_t^d)^T$. The Green's function G_{soc} is given by

$$G_{\text{soc}}(r, r') = \sum_s \frac{|\psi_s(r)\rangle \langle \psi_s(r')|}{E - \epsilon_s + i\delta}, \quad (C4)$$

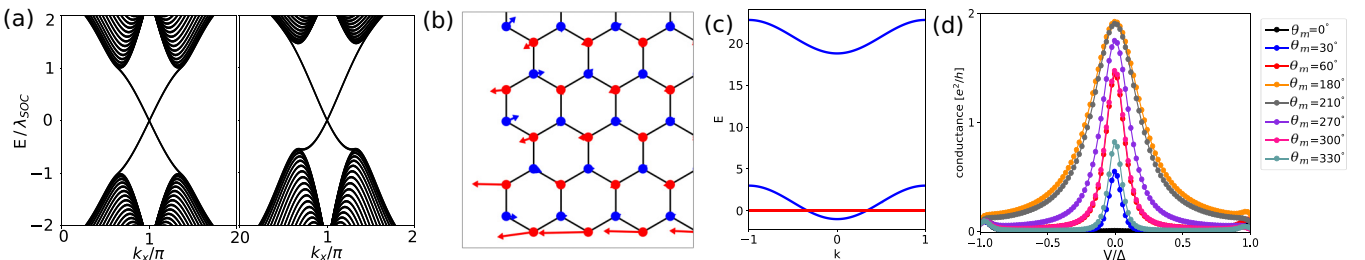


FIG. 6. (a) The left and right figures are the electronic band structure along the zigzag of the system without and with the next-nearest hopping term, respectively. (b) The distribution of Majorana spin polarization in the system with the next-nearest hopping term. (c) Band structure of the lead. (d) The conductance of the system without chiral symmetry was probed by the lead with different polarization directions.

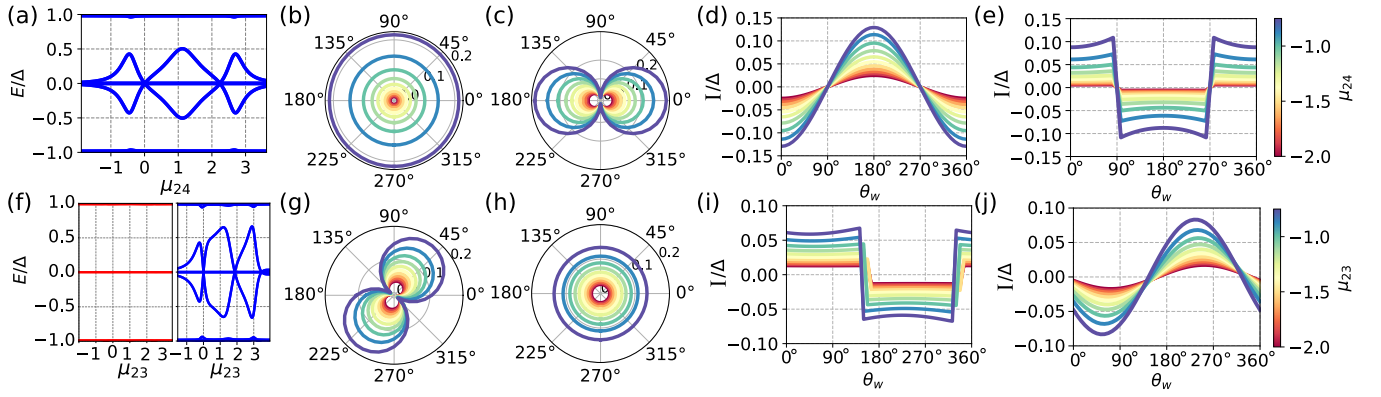


FIG. 7. (a) and (f) are the Andreev level as the function of chemical potential μ_{24} and μ_{23} in the wires N_{24} and N_{23} , respectively. The red (blue) curves in (f) correspond to $\lambda = 0$ and $\lambda \neq 0$, respectively. (b) and (c) are the lowest positive eigenenergy as a function of θ_w at $\phi = 0$ and $\phi = \pi$ of JJ_a , respectively. (d) and (e) are the Josephson current at $\phi = 0$ and $\phi = \pi$ as a function of magnetic field direction of JJ_a . (g) and (h) are the lowest positive eigenenergy as a function of θ_w at $\phi = 0$ and $\phi = \pi$ of JJ_b , respectively. (i) and (j) are the Josephson current at $\phi = 0$ and $\phi = \pi$ as a function of magnetic field direction of JJ_b .

where $\epsilon_s = -2 \cos(k) \sqrt{t_w^2 + \lambda^2}$ is the eigenenergy of the wire. $|\psi_s\rangle$ ($s = \rightarrow, \leftarrow$) are the eigenfunction of the wire satisfying $|\psi_s(0)\rangle = |\psi_s(l+1)\rangle = 0$ (l is the length of wire), which can be expressed as

$$\begin{aligned} \psi_{\rightarrow} &= \frac{1}{\sqrt{2}} [1, 1]^T e^{-i\frac{\delta k}{2}r} \sin kr, \\ \psi_{\leftarrow} &= \frac{1}{\sqrt{2}} [1, -1]^T e^{i\frac{\delta k}{2}r} \sin kr, \end{aligned} \quad (C5)$$

where $k = n\pi/(l+1)$. Thus, the effective coupling Hamiltonian in Majorana space takes

$$\tilde{H}_J = \tilde{t}' \gamma_i \Psi_i^\dagger(u) \begin{bmatrix} e^{\frac{i}{2}(\phi_{s0} + \beta_{s_x})} & 0 \\ 0 & -e^{-\frac{i}{2}(\phi_{s0} + \beta_{s_x})} \end{bmatrix} \Psi_j(d) \gamma_j \quad (C6)$$

with $\tilde{t}' = t_w^2 \sum_k \sin(ka) \sin(kl)/(E - 2 \cos(k) \sqrt{t_w^2 + \lambda^2})$ and $\beta = 2m\lambda l/\hbar$. $\Psi_{i(j)=1,2,3,4}(r)$ are the wave functions of the MCMs $\gamma_{i(j)}$ at site r . We first consider the MCMs γ_2, γ_4 which are localized at corner 2 and corner 4. Under in-plane magnetic field along the $(\cos \theta_w, \sin \theta_w, 0)$ direction, the wave function of the two MCMs are given by

$$\Psi_2(u) = \rho \begin{bmatrix} \phi_{2,u} \\ \phi_{2,u}^* \end{bmatrix}; \Psi_4(d) = \rho \begin{bmatrix} i\phi_{4,d} \\ -i\phi_{4,d}^* \end{bmatrix} \quad (C7)$$

with

$$\phi_{2,u} = \begin{bmatrix} e^{-\frac{i}{2}(\theta_w + \frac{3\pi}{2} + \alpha_c)} \\ e^{\frac{i}{2}(\theta_w + \frac{3\pi}{2} + \alpha_c)} \end{bmatrix}; \phi_{4,d} = \begin{bmatrix} e^{-\frac{i}{2}(\theta_w + \frac{\pi}{2} - \alpha_c)} \\ e^{\frac{i}{2}(\theta_w + \frac{\pi}{2} - \alpha_c)} \end{bmatrix}, \quad (C8)$$

where α_c describe the polarization deviation from the perpendicular direction to the magnetic field due to the chiral symmetry breaking. Accordingly, we project the Josephson junction Hamiltonian into the low energy Majorana Hilbert space as

$$\tilde{H}_a = i\tilde{t}' \gamma_2 \gamma_4 \left(\sin \alpha_c \cos \frac{\beta}{2} \cos \frac{\phi}{2} - \cos \theta_w \sin \frac{\beta}{2} \sin \frac{\phi}{2} \right) \quad (C9)$$

with $\tilde{t} = 4\rho^2 \tilde{t}'$ and the associated Josephson current

$$I_a = \pm \frac{e\tilde{t}}{\hbar} \left(\sin \alpha_c \cos \frac{\beta}{2} \sin \frac{\phi}{2} - \cos \theta_w \sin \frac{\beta}{2} \cos \frac{\phi}{2} \right). \quad (C10)$$

According to Eq. (C9), at $\phi = 0$, the amplitude of Majorana coupling in JJ_a is independent of the magnetic field direction. To verify this result, we perform the numerical calculations in the low-energy Hamiltonian of bismuthene. The magnitude of Majorana coupling remains constant with varying θ_w [Fig. 7(b)], which is consistent with the theoretical analysis. At $\phi = \pi$, the Majorana coupling oscillates with θ_w and vanishes at $\theta_w = \pm\pi/2$ [Fig. 7(c)], which is protected by mirror symmetry. Meanwhile, the mirror symmetry also let the Josephson current vanished at $\theta_w = \pm\pi/2$, $\phi = 0$ and $\phi = \pi$ [Figs. 7(d) and 7(e)]. When $\theta_w \neq \pm\pi/2$, the Josephson current magnitude at $\phi = 0$ oscillates and reaches its maximal at $\theta_w = 0, \pi$, but remains constant at $\phi = \pi$. For JJ_b , the MCMs are related through the inversion operator. Thus, the wave function of γ_3 can be expressed as

$$\Psi_3(d) = \rho \begin{bmatrix} \phi_{3,d} \\ \phi_{3,d}^* \end{bmatrix} \quad (C11)$$

with

$$\phi_{3,d} = \begin{bmatrix} e^{-\frac{i}{2}(\theta_w + \frac{3\pi}{2} + \alpha_c)} \\ e^{\frac{i}{2}(\theta_w + \frac{3\pi}{2} + \alpha_c)} \end{bmatrix}. \quad (C12)$$

The effective Hamiltonian in Majorana space of JJ_b takes

$$\tilde{H}_b = i\tilde{t}' \gamma_2 \gamma_3 \left(\cos \frac{\beta}{2} \sin \frac{\phi}{2} + \sin(\theta_w + \alpha_c) \sin \frac{\beta}{2} \cos \frac{\phi}{2} \right). \quad (C13)$$

The energy level of Eq. (C13) crosses at

$$\phi_c = -2 \arctan(\sin(\theta_w + \alpha_c) \tan(\beta/2)). \quad (C14)$$

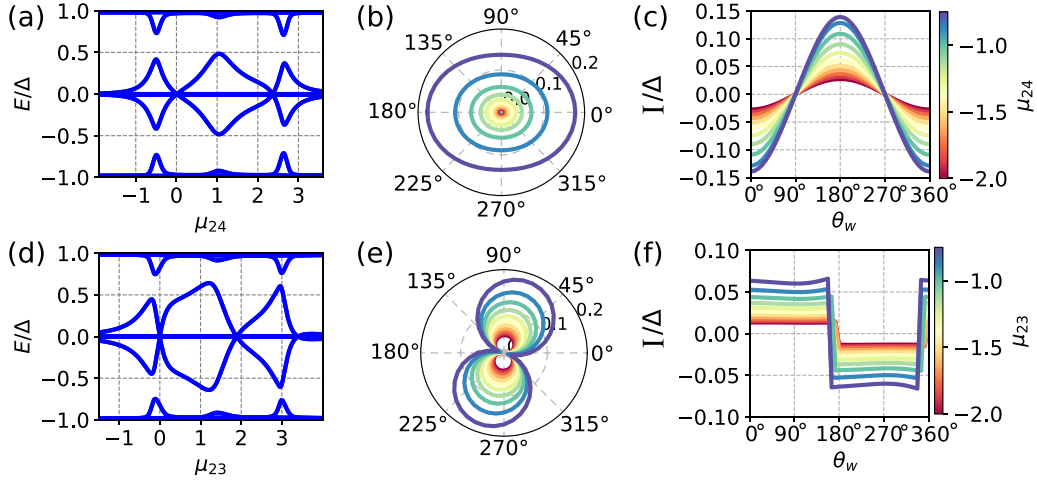


FIG. 8. (a) and (d) are the Andreev level as the function of chemical potential μ_{24} and μ_{23} in the wires N_{24} and N_{23} , respectively. (b) and (e) are the lowest positive eigenenergy at $\phi = 0$ as a function of θ_w in JJ_a and JJ_b , respectively. (c) and (f) are the Josephson current at $\phi = 0$ as a function of θ_w in JJ_a and JJ_b , respectively.

Consequently, the occupied Andreev levels take the form

$$E_b^- = \begin{cases} -\tilde{t}(\cos \frac{\beta}{2} \sin \frac{\phi}{2} + \sin(\theta_w + \alpha_c) \sin \frac{\beta}{2} \cos \frac{\phi}{2}) & (\phi < \phi_c) \\ \tilde{t}(\cos \frac{\beta}{2} \sin \frac{\phi}{2} + \sin(\theta_w + \alpha_c) \sin \frac{\beta}{2} \cos \frac{\phi}{2}) & (\phi > \phi_c) \end{cases} \quad (C15)$$

The related currents of the Josephson junction JJ_b at $\phi = 0$ is

$$I_b = \frac{2e}{\hbar} \frac{E_b^-(\delta\phi) - E_b^-(-\delta\phi)}{2\delta\phi} = \begin{cases} -\frac{e\tilde{t}}{\hbar} \cos \frac{\beta}{2} & (0 < \phi_c) \\ \frac{e\tilde{t}}{\hbar} \cos \frac{\beta}{2} & (0 > \phi_c) \end{cases} \quad (C16)$$

According to Eq. (C16) the form of I_b depends on the sign of ϕ_c . Fixing the SOC strength with $\tan(\beta/2) > 0$, the sign ϕ_c is

equivalent to the sign $\sin(\theta_w + \alpha_c)$ according to Eq. (C14). Consequently, current I_b can be simplified as

$$I_b = \frac{e\tilde{t}}{\hbar} \text{sgn}(\sin(\theta_w + \alpha_c)) \cos \frac{\beta}{2}. \quad (C17)$$

Thus, at $\phi = 0$, turning off Rashba SOC of the wire, i.e., $\beta = 0$, the MCMs decouple at any chemical potential of N_{23} as shown in Fig. 7(f). Consequently, to realize the Majorana coupling in JJ_b , we must consider wire N_{23} with Rashba SOC. At $\phi = 0$, the amplitude of the Majorana coupling oscillate with θ_w and vanish at $\theta_w + \alpha_c = 0(\pi)$ as shown in Fig. 7(g). The associative Josephson current remains unchanged and only change sign when $\theta_w + \alpha_c$ across $0, \pi$ in Fig. 7(i). At $\phi = \pi$, the magnitude of Majorana coupling remains constant

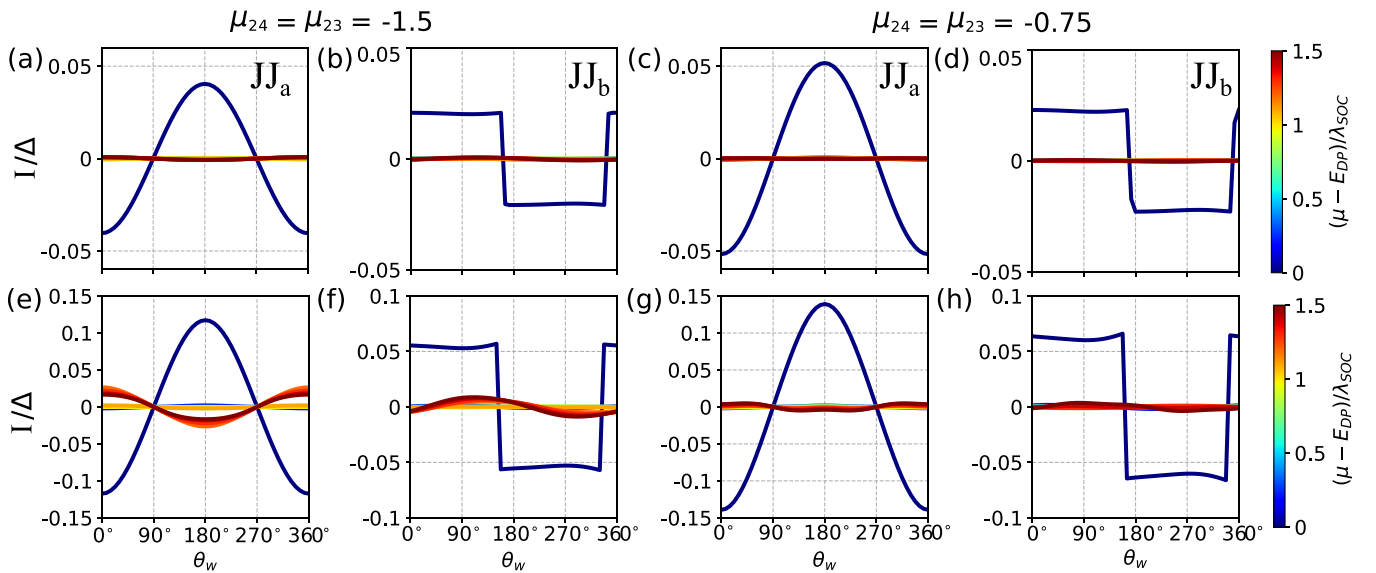


FIG. 9. The function between current at $\phi = 0$ and the direction of magnetic field θ_w for the Josephson junction without [(a)–(d)] and with [(e)–(h)] considering d_0 term. In Josephson junctions JJ_a and JJ_b , the current are calculated with the different magnitude of chemical potentials of the normal wire, and the curves with different colors indicate the magnitude of chemical potential in the superconductor region, as illustrated by colorbars.

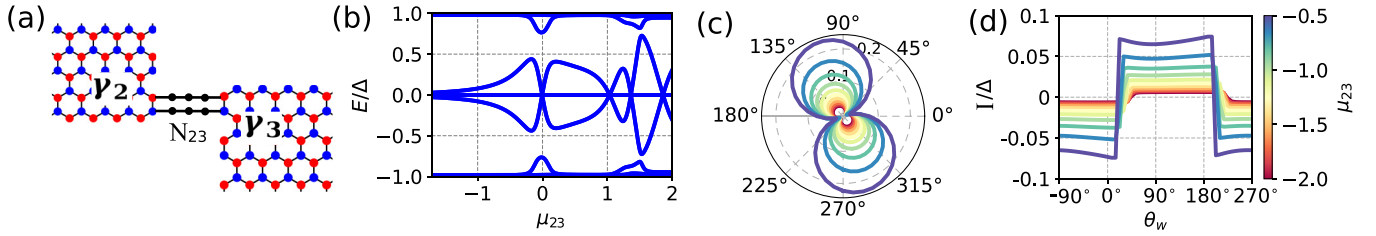


FIG. 10. (a) The configuration of JJ_b . (b) Andreev level as a function of μ_{23} in the wire N_{23} at $\phi = 0$. (c) and (d) are the lowest positive eigenenergy and Josephson current as a function of θ_w .

and Josephson current oscillates with varying θ_w . Notably, considering the uniform Zeeman term, these features are virtually unchanged as shown in the main text.

2. Topological ϕ_0 junction constructed by HOTSCs without chiral symmetry

Now, we consider the Josephson junction construct by HOTSCs that break chiral symmetry. To break chiral symmetry, we consider the next-nearest-neighbor hopping term. The polarization direction of MCMs deflects but is still roughly perpendicular to the direction of the magnetic field as discussed above. That is to say, it only changes the deflection angle α_c . To numerically verify the result, we still plot the magnitude of Majorana coupling and the Josephson current amplitude as the function of θ_w at $\phi = 0$. As shown in Fig. 8, our results generally remain valid.

3. Josephson current in topological and trivial ϕ_0 junction

In this section, we consider the change of Josephson current in the ϕ_0 junction when the superconducting regions are under different topological conditions. Taking $M = 2\Delta$,

for the superconducting region, the edge states along zigzag direction undergo a phase transition and entry into the trivial superconducting region when tuning the chemical potential μ away from the Dirac point [25]. Consequently, tuning μ leads the Josephson junction to leave the topological region and form a trivial ϕ_0 junction. As shown in Figs. 9(a) and 9(b), the Josephson current in JJ_a becomes much smaller in the trivial region. It is worth noting that the induced Josephson currents in JJ_b behave quite differently. As shown in Figs. 9(c) and 9(d), the Josephson current is virtually unchanged under varying θ_w in the topological region, while oscillating in the trivial region. This may provide evidence for the system entering into the topological region.

4. JJ_b constructed by connecting HOTSCs along armchair

In this section, we study the θ_w dependence of the Josephson current amplitude at $\phi = 0$, which is constructed by connecting HOTSCs along the armchair direction [Fig. 10(a)]. In this configuration, the spin texture of the MCMs at the end of the normal does not satisfy the mirror symmetry. Josephson coupling energy still shows a strong magnetic field direction dependence and the current amplitude remains insensitive to magnetic field direction as shown in Figs. 10(c) and 10(d).

- [1] D. A. Ivanov, *Phys. Rev. Lett.* **86**, 268 (2001).
- [2] A. Kitaev, *Ann. Phys.* **303**, 2 (2003).
- [3] C. Nayak, S. H. Simon, A. Stern, M. Freedman, and S. Das Sarma, *Rev. Mod. Phys.* **80**, 1083 (2008).
- [4] L. Fu and C. L. Kane, *Phys. Rev. Lett.* **100**, 096407 (2008).
- [5] J. D. Sau, R. M. Lutchyn, S. Tewari, and S. Das Sarma, *Phys. Rev. Lett.* **104**, 040502 (2010).
- [6] R. M. Lutchyn, J. D. Sau, and S. Das Sarma, *Phys. Rev. Lett.* **105**, 077001 (2010).
- [7] J. Alicea, Y. Oreg, G. Refael, F. von Oppen, and M. P. A. Fisher, *Nat. Phys.* **7**, 412 (2011).
- [8] J. Alicea, *Rep. Prog. Phys.* **75**, 076501 (2012).
- [9] C. Beenakker, *Annu. Rev. Condens. Matter Phys.* **4**, 113 (2013).
- [10] S. D. Sarma, M. Freedman, and C. Nayak, *npj Quantum Inf.* **1**, 15001 (2015).
- [11] S. R. Elliott and M. Franz, *Rev. Mod. Phys.* **87**, 137 (2015).
- [12] R. Aguado and L. P. Kouwenhoven, *Phys. Today* **73**(6), 44 (2020).
- [13] J. Langbehn, Y. Peng, L. Trifunovic, F. von Oppen, and P. W. Brouwer, *Phys. Rev. Lett.* **119**, 246401 (2017).
- [14] Z. Yan, F. Song, and Z. Wang, *Phys. Rev. Lett.* **121**, 096803 (2018).
- [15] Y. Wang, M. Lin, and T. L. Hughes, *Phys. Rev. B* **98**, 165144 (2018).
- [16] Q. Wang, C.-C. Liu, Y.-M. Lu, and F. Zhang, *Phys. Rev. Lett.* **121**, 186801 (2018).
- [17] C.-H. Hsu, P. Stano, J. Klinovaja, and D. Loss, *Phys. Rev. Lett.* **121**, 196801 (2018).
- [18] T. Liu, J. J. He, and F. Nori, *Phys. Rev. B* **98**, 245413 (2018).
- [19] Y. Volpez, D. Loss, and J. Klinovaja, *Phys. Rev. Lett.* **122**, 126402 (2019).
- [20] R.-X. Zhang, W. S. Cole, and S. Das Sarma, *Phys. Rev. Lett.* **122**, 187001 (2019).
- [21] X. Zhu, *Phys. Rev. Lett.* **122**, 236401 (2019).
- [22] M. Ezawa, *Phys. Rev. B* **100**, 045407 (2019).
- [23] S. A. A. Ghorashi, X. Hu, T. L. Hughes, and E. Rossi, *Phys. Rev. B* **100**, 020509(R) (2019).
- [24] S. Franca, D. V. Efremov, and I. C. Fulga, *Phys. Rev. B* **100**, 075415 (2019).
- [25] X.-H. Pan, K.-J. Yang, L. Chen, G. Xu, C.-X. Liu, and X. Liu, *Phys. Rev. Lett.* **123**, 156801 (2019).

- [26] R.-X. Zhang, W. S. Cole, X. Wu, and S. Das Sarma, *Phys. Rev. Lett.* **123**, 167001 (2019).
- [27] Z. Yan, *Phys. Rev. Lett.* **123**, 177001 (2019).
- [28] Z. Yan, *Phys. Rev. B* **100**, 205406 (2019).
- [29] A. Tiwari, M.-H. Li, B. A. Bernevig, T. Neupert, and S. A. Parameswaran, *Phys. Rev. Lett.* **124**, 046801 (2020).
- [30] K. Laubscher, D. Loss, and J. Klinovaja, *Phys. Rev. Research* **2**, 013330 (2020).
- [31] Y.-J. Wu, J. Hou, Y.-M. Li, X.-W. Luo, X. Shi, and C. Zhang, *Phys. Rev. Lett.* **124**, 227001 (2020).
- [32] M. Kheirkhah, Z. Yan, Y. Nagai, and F. Marsiglio, *Phys. Rev. Lett.* **125**, 017001 (2020).
- [33] S. A. A. Ghorashi, T. L. Hughes, and E. Rossi, *Phys. Rev. Lett.* **125**, 037001 (2020).
- [34] S.-B. Zhang, A. Calzona, and B. Trauzettel, *Phys. Rev. B* **102**, 100503(R) (2020).
- [35] S.-B. Zhang, W. B. Rui, A. Calzona, S.-J. Choi, A. P. Schnyder, and B. Trauzettel, *Phys. Rev. Research* **2**, 043025 (2020).
- [36] K. Plekhanov, N. Müller, Y. Volpez, D. M. Kennes, H. Schoeller, D. Loss, and J. Klinovaja, *Phys. Rev. B* **103**, L041401 (2021).
- [37] Y.-X. Li and T. Zhou, *Phys. Rev. B* **103**, 024517 (2021).
- [38] A. K. Ghosh, T. Nag, and A. Saha, *Phys. Rev. B* **103**, 045424 (2021).
- [39] A. K. Ghosh, T. Nag, and A. Saha, *Phys. Rev. B* **103**, 085413 (2021).
- [40] B.-X. Li and Z. Yan, *Phys. Rev. B* **103**, 064512 (2021).
- [41] M. F. Lapa, M. Cheng, and Y. Wang, *arXiv:2103.03893* (2021).
- [42] M. Kheirkhah, Z. Yan, and F. Marsiglio, *Phys. Rev. B* **103**, L140502 (2021).
- [43] L. Chen, B. Liu, G. Xu, and X. Liu, *Phys. Rev. Research* **3**, 023166 (2021).
- [44] J. Niu, T. Yan, Y. Zhou, Z. Tao, X. Li, W. Liu, L. Zhang, H. Jia, S. Liu, Z. Yan, Y. Chen, and D. Yu, *Sci. Bull.* **66**, 1168 (2021).
- [45] X.-J. Luo, X.-H. Pan, and X. Liu, *Phys. Rev. B* **104**, 104510 (2021).
- [46] Y. Tan, Z.-H. Huang, and X.-J. Liu, *Phys. Rev. B* **105**, L041105 (2022).
- [47] D. Zhu, B.-X. Li, and Z. Yan, *arXiv:2112.00761* (2021).
- [48] V. Mourik, K. Zuo, S. M. Frolov, S. R. Plissard, E. P. A. M. Bakkers, and L. P. Kouwenhoven, *Science* **336**, 1003 (2012).
- [49] M. T. Deng, C. L. Yu, G. Y. Huang, M. Larsson, P. Caroff, and H. Q. Xu, *Nano Lett.* **12**, 6414 (2012).
- [50] A. Das, Y. Ronen, Y. Most, Y. Oreg, M. Heiblum, and H. Shtrikman, *Nat. Phys.* **8**, 887 (2012).
- [51] S. Nadj-Perge, I. K. Drozdov, J. Li, H. Chen, S. Jeon, J. Seo, A. H. MacDonald, B. A. Bernevig, and A. Yazdani, *Science* **346**, 602 (2014).
- [52] J.-P. Xu, M.-X. Wang, Z. L. Liu, J.-F. Ge, X. Yang, C. Liu, Z. A. Xu, D. Guan, C. L. Gao, D. Qian, Y. Liu, Q.-H. Wang, F.-C. Zhang, Q.-K. Xue, and J.-F. Jia, *Phys. Rev. Lett.* **114**, 017001 (2015).
- [53] S. M. Albrecht, A. P. Higginbotham, M. Madsen, F. Kuemmeth, T. S. Jespersen, J. Nygård, P. Krogstrup, and C. M. Marcus, *Nature (London)* **531**, 206 (2016).
- [54] D. Wang, L. Kong, P. Fan, H. Chen, S. Zhu, W. Liu, L. Cao, Y. Sun, S. Du, J. Schneeloch, R. Zhong, G. Gu, L. Fu, H. Ding, and H.-J. Gao, *Science* **362**, 333 (2018).
- [55] Q. Liu, C. Chen, T. Zhang, R. Peng, Y.-J. Yan, C.-H.-P. Wen, X. Lou, Y.-L. Huang, J.-P. Tian, X.-L. Dong, G.-W. Wang, W.-C. Bao, Q.-H. Wang, Z.-P. Yin, Z.-X. Zhao, and D.-L. Feng, *Phys. Rev. X* **8**, 041056 (2018).
- [56] M. Chen, X. Chen, H. Yang, Z. Du, X. Zhu, E. Wang, and H.-H. Wen, *Nat. Commun.* **9**, 970 (2018).
- [57] F. Pientka, G. Kells, A. Romito, P. W. Brouwer, and F. von Oppen, *Phys. Rev. Lett.* **109**, 227006 (2012).
- [58] J. Liu, A. C. Potter, K. T. Law, and P. A. Lee, *Phys. Rev. Lett.* **109**, 267002 (2012).
- [59] W. S. Cole, J. D. Sau, and S. Das Sarma, *Phys. Rev. B* **94**, 140505(R) (2016).
- [60] C.-X. Liu, J. D. Sau, T. D. Stanescu, and S. Das Sarma, *Phys. Rev. B* **96**, 075161 (2017).
- [61] S. Das Sarma and H. Pan, *Phys. Rev. B* **103**, 195158 (2021).
- [62] H. Pan, C.-X. Liu, M. Wimmer, and S. Das Sarma, *Phys. Rev. B* **103**, 214502 (2021).
- [63] H. Pan and S. Das Sarma, *Phys. Rev. B* **104**, 054510 (2021).
- [64] D. Sticlet, C. Bena, and P. Simon, *Phys. Rev. Lett.* **108**, 096802 (2012).
- [65] J. J. He, T. K. Ng, P. A. Lee, and K. T. Law, *Phys. Rev. Lett.* **112**, 037001 (2014).
- [66] P. Kotetes, D. Mendler, A. Heimes, and G. Schön, *Phys. E* **74**, 614 (2015).
- [67] H.-H. Sun, K.-W. Zhang, L.-H. Hu, C. Li, G.-Y. Wang, H.-Y. Ma, Z.-A. Xu, C.-L. Gao, D.-D. Guan, Y.-Y. Li, C. Liu, D. Qian, Y. Zhou, L. Fu, S.-C. Li, F.-C. Zhang, and J.-F. Jia, *Phys. Rev. Lett.* **116**, 257003 (2016).
- [68] S. Jeon, Y. Xie, J. Li, Z. Wang, B. A. Bernevig, and A. Yazdani, *Science* **358**, 772 (2017).
- [69] M. Serina, D. Loss, and J. Klinovaja, *Phys. Rev. B* **98**, 035419 (2018).
- [70] S. Głodzik, N. Sedlmayr, and T. Domański, *Phys. Rev. B* **102**, 085411 (2020).
- [71] Y. Asano and Y. Tanaka, *Phys. Rev. B* **87**, 104513 (2013).
- [72] H. Ebisu, K. Yada, H. Kasai, and Y. Tanaka, *Phys. Rev. B* **91**, 054518 (2015).
- [73] X. Liu, J. D. Sau, and S. Das Sarma, *Phys. Rev. B* **92**, 014513 (2015).
- [74] K. Zhang, J. Zeng, Y. Ren, and Z. Qiao, *Phys. Rev. B* **96**, 085117 (2017).
- [75] L. Chen, Y.-H. Wu, and X. Liu, *Phys. Rev. B* **99**, 165307 (2019).
- [76] D. M. Badiane, M. Houzet, and J. S. Meyer, *Phys. Rev. Lett.* **107**, 177002 (2011).
- [77] X. Liu, X. Li, D.-L. Deng, X.-J. Liu, and S. Das Sarma, *Phys. Rev. B* **94**, 014511 (2016).
- [78] M. Guigou, N. Sedlmayr, J. M. Aguiar-Hualde, and C. Bena, *Europhys. Lett.* **115**, 47005 (2016).
- [79] E. Prada, R. Aguado, and P. San-Jose, *Phys. Rev. B* **96**, 085418 (2017).
- [80] A. A. Aligia, D. Pérez Daroca, and L. Arrachea, *Phys. Rev. Lett.* **125**, 256801 (2020).
- [81] B. van Heck, A. R. Akhmerov, F. Hassler, M. Burrello, and C. W. J. Beenakker, *New J. Phys.* **14**, 035019 (2012).
- [82] X.-J. Liu, C. L. M. Wong, and K. T. Law, *Phys. Rev. X* **4**, 021018 (2014).
- [83] A. Stern and E. Berg, *Phys. Rev. Lett.* **122**, 107701 (2019).
- [84] C. L. Kane and E. J. Mele, *Phys. Rev. Lett.* **95**, 146802 (2005).
- [85] C. L. Kane and E. J. Mele, *Phys. Rev. Lett.* **95**, 226801 (2005).

- [86] B. B. Andrei, L. Hughes Taylor, and Z. Shou-Cheng, *Science* **314**, 1757 (2006).
- [87] M. Z. Hasan and C. L. Kane, *Rev. Mod. Phys.* **82**, 3045 (2010).
- [88] X.-L. Qi and S.-C. Zhang, *Rev. Mod. Phys.* **83**, 1057 (2011).
- [89] G. Li, W. Hanke, E. M. Hankiewicz, F. Reis, J. Schäfer, R. Claessen, C. Wu, and R. Thomale, *Phys. Rev. B* **98**, 165146 (2018).
- [90] G.-F. Zhang, Y. Li, and C. Wu, *Phys. Rev. B* **90**, 075114 (2014).
- [91] F. Reis, G. Li, L. Dudy, M. Bauernfeind, S. Glass, W. Hanke, R. Thomale, J. Schäfer, and R. Claessen, *Science* **357**, 287 (2017).
- [92] C. W. Groth, M. Wimmer, A. R. Akhmerov, and X. Waintal, *New J. Phys.* **16**, 063065 (2014).
- [93] J. D. Sau, D. J. Clarke, and S. Tewari, *Phys. Rev. B* **84**, 094505 (2011).
- [94] D. Pekker, C.-Y. Hou, V. E. Manucharyan, and E. Demler, *Phys. Rev. Lett.* **111**, 107007 (2013).
- [95] B. van Heck, T. Hyart, and C. W. J. Beenakker, *Phys. Scr.* **2015**, 014007 (2015).
- [96] D. Aasen, M. Hell, R. V. Mishmash, A. Higginbotham, J. Danon, M. Leijnse, T. S. Jespersen, J. A. Folk, C. M. Marcus, K. Flensberg, and J. Alicea, *Phys. Rev. X* **6**, 031016 (2016).
- [97] S. Vijay and L. Fu, *Phys. Rev. B* **94**, 235446 (2016).
- [98] T. Karzig, C. Knapp, R. M. Lutchyn, P. Bonderson, M. B. Hastings, C. Nayak, J. Alicea, K. Flensberg, S. Plugge, Y. Oreg, C. M. Marcus, and M. H. Freedman, *Phys. Rev. B* **95**, 235305 (2017).
- [99] D. Litinski and F. von Oppen, *Phys. Rev. B* **96**, 205413 (2017).
- [100] J. P. T. Stenger, M. Hatridge, S. M. Frolov, and D. Pekker, *Phys. Rev. B* **99**, 035307 (2019).
- [101] D. B. Szombati, S. Nadj-Perge, D. Car, S. R. Plissard, E. P. A. M. Bakkers, and L. P. Kouwenhoven, *Nat. Phys.* **12**, 568 (2016).
- [102] L. Dell’Anna, A. Zazunov, R. Egger, and T. Martin, *Phys. Rev. B* **75**, 085305 (2007).
- [103] A. Zazunov, R. Egger, T. Jonckheere, and T. Martin, *Phys. Rev. Lett.* **103**, 147004 (2009).
- [104] A. Brunetti, A. Zazunov, A. Kundu, and R. Egger, *Phys. Rev. B* **88**, 144515 (2013).
- [105] F. Wilczek and A. Zee, *Phys. Rev. Lett.* **52**, 2111 (1984).
- [106] R. Yu, X. L. Qi, A. Bernevig, Z. Fang, and X. Dai, *Phys. Rev. B* **84**, 075119 (2011).
- [107] K. Snizhko, R. Egger, and Y. Gefen, *Phys. Rev. Lett.* **123**, 060405 (2019).